Modelling interaction of incompressible fluids and deformable particles with the Material Point Method

Rachel Gelet, Giang Nguyen, Pierre Rognon

Modelling interaction of incompressible fluids and deformable particles with the Material Point Method

Rachel Gelet [1,3]*, Giang Nguyen[2,3], Pierre Rognon[3]

[1] GeM laboratory, University of Nantes, 58 rue Michel Ange, BP 420, 44606, Saint-Nazaire Cedex, France.
[2] School of Civil, Environmental and Mining Engineering, The University of Adelaide, Adelaide, SA 5005, Australia.
[3] School of Civil Engineering, The University of Sydney, Sydney, NSW, 2006 Australia.

December 4, 2015

Abstract

The long-range interaction between one incompressible fluid surrounding solid objects is quite common and includes suspensions, sedimentation, fluid motion around obstacles, and erosion. Concerning the active research field of fluid-solid interactions, the challenging point nowadays is to describe the fluid dynamics in the pore space of soils or concrete samples and to establish a full coupling between the fluid and the movable deformable solid phase. This paper describes an extension of the material-point method (MPM) to modelling the interactions of incompressible fluids and multi-body deformable particles, which are discretized by a collection of unconnected, Lagrangian, material points. Primary variables, such as displacement, velocity, pressure and acceleration, and material variables, such as mass, stress and strain are associated with these points. To solve the equations of motion, data mapped from the material points are used to update variables on a background Eulerian mesh. The mesh solution is then mapped back to material points. This standard particle-like method treats all materials in a uniform way, thus avoiding complicated mesh construction and automatically possessing a no-slip contact algorithm at no additional cost.

*rachel.gelet@univ-nantes.fr

In this study, the solid phase is treated as elastic, but general inelastic descriptions can also be later included to explore the interaction with the fluid phase. On the other hand, problems of incompressibility introduce numerical difficulties which need to be treated. Hence the enhanced strain method is adapted to the MPM analysis and specified to the study of long-range hydrodynamic interactions between incompressible fluid and solid deformable objects. Numerical examples including a fluid flow around an obstacle, the collapse of a water column and a sedimentation test are used to illustrate the proposed approach and its potential. The results of the MPM are compared with those obtained with classical FEM, XFEM and a modified immersed boundary method. In addition, the MPM results also compare well with existing experimental measurements of the collapsing water problem.

Keywords: Material Point Method (MPM); Fluid-Solid Interaction (FSI); Incompressible fluid; Enhanced Strain Method

1 Introduction

The long-range interaction between one incompressible fluid surrounding solid objects is quite common and includes suspensions, sedimentation, fluid motion around obstacles, and internal erosion. For example, the modelling of internal erosion at the scale of pore constrictions requires a complete description of both the grains/particles and the fluid within the pores [12]. While continuous methods are used at the scale of civil engineering structures, such as embankment dams [4] or sandstones reservoirs [19], discrete and micromechanical methods are being developed to describe the fluid dynamics in the pore space of soils and to establish a full coupling between the fluid and the movable *deformable* solid phase.

Concerning the active research field of fluid-solid interactions (FSI), a number of numerical methods are been developed [10]: Eulerian-Eulerian, Lagrangian-Lagrangian and Eulerian-Lagrangian methods.

Lagrangian-Lagrangian methods are based on the idea that calculation points (i.e. nodes or particles) of both phases are fixed to the domain being modelled throughout the analysis. This leads to the disappearance of convective terms in the governing equations of the model. The codes are then conceptually simpler and faster in this aspect, in contrast to Eulerian-Eulerian approaches. Since nodes/particles are placed and remain on material surfaces, interface tracking should be trivial. Those methods can be further subclassified into grid-based methods and meshless/particles methods. Un-

like grid-based methods [1, 15], meshless or particles methods approximate partial differential equations only based on a set of points without the need for an additional mesh (no nodal connectivity is introduced) [5]. The advantages of those methods, absence of a mesh, continuity of the shape functions and convergence, are damped by a few difficulties such as the application of essential boundary conditions, the computational effort and a certain sensitivity of the solutions to the inhomogeneous repartition of the particles.

The material point method (MPM) is a particle method that is based on the approximation of the weak form of partial differential equations [23, 24]. Aside from the advantages from the Lagrangian frame of reference and from the particle approach in terms of interface tracking, the key characteristic of the MPM is to use a background finite element mesh to solve the governing equations. Since this mesh does not carry any information, a regular grid can be utilized throughout the simulations. Thereby, the MPM combines the good features of both the finite element methods and the purely particle based methods. Finally, the MPM enjoys a single-valued velocity field which allows a natural treatment of no-slip contact and hence straightforward simulations of multi-phase materials.

Regarding geomechanical problems, different numerical methods have been applied to FSI problems with some success [2, 17, 12]. However, several drawbacks remain and there exists a need for a method combining the possibility of accurate representation of large deformation and displacement, together with an easy representation of solid-fluid interfaces and particles of random size and shape. At the moment, the use of the MPM is in the development of the research activities of our group [20, 8, 16] and pertains to a wider project targeting the development of grain contact laws in a fluid environment for the DEM. In this context, this work is a first step to establish a numerical framework and tools for the investigation of fluid-solid interactions, towards the ultimate goals of exploring immersed grains and developing corresponding DEM contact laws in the next step.

This paper describes an extension of the MPM to model the interactions of incompressible fluids and multi-body deformable particles. In the second section of this article, the governing equations are presented and the framework of the MPM is briefly addressed. The third section is devoted to the weak form of the governing equations, in which an enhanced strain element is used to represent the incompressible fluid phase. To highlight the potentials of the proposed method, we present in a final section three numerical examples: a fluid flow around an obstacle, the collapse of a water column and a sedimentation test.

2 Governing equations

In this section, the fundamental equations governing the problem are introduced: i.e. balance equations, and constitutive laws for the solid and liquid phases. Prior to the weak form, the MPM framework is presented which implies the spatial discetisation of each phases with material points endowed with point masses.

Motion of a continuum is governed by conservation of momentum and mass. Let's introduce the following global notations: ρ is the mass density, $\mathbf{a}$ is the acceleration, $\mathbf{v}$ is the velocity, $\boldsymbol{\sigma}$ is a symmetric Cauchy stress tensor, and $\mathbf{b}$ is the specific body force. For the whole domain (both the fluid and the solid phases), the global balance of momentum in the Lagrangian frame of reference and the global balance of mass read,

$$\begin{aligned} \operatorname{div}\boldsymbol{\sigma} + \rho\mathbf{b} &= \rho\mathbf{a}\,, \\ \dot{\rho} &= -\rho \operatorname{div}\mathbf{v}\,, \end{aligned} \tag{1}$$

For solid and fluid material points, the general form of the constitutive equation relates the stress rate, or the stress, to the strain rate *via* a tangent modulus,

$$\begin{aligned} \dot{\boldsymbol{\sigma}}_s &= \mathbf{T}_s : \dot{\boldsymbol{\epsilon}}\,, \\ \boldsymbol{\sigma}_f &= \lambda_f \operatorname{tr}(\dot{\boldsymbol{\epsilon}})\,\mathbf{I} + 2\mu_f\,\dot{\boldsymbol{\epsilon}} = \mathbf{T}_f : \dot{\boldsymbol{\epsilon}}\,, \end{aligned} \tag{2}$$

with $\lambda_f = 2\nu_f\mu_f/(1-2\nu_f)$ the Lamé parameter, μ_f the dynamic viscosity and ν_f the Poisson's ratio. Clearly, as $\nu_f \to \frac{1}{2}$, the Lamé parameter approaches infinity, so that nearly incompressible cases are characterised by $\mu_f \ll \lambda_f$. For simplicity, constitutive equations are presented in terms of the small deformation theory, and the strain rate tensor is related to the velocity through,

$$\dot{\boldsymbol{\epsilon}} = \frac{1}{2}\left[\nabla\mathbf{v} + (\nabla\mathbf{v})^{\mathrm{T}}\right] = \nabla^{*}\mathbf{v}\,. \tag{3}$$

More general responses for the solid have already been implemented in the MPM [26, 16, 13] and are left for future work.

This work pertains to the classical MPM framework [23, 24], so that the governing equations are solved in a Lagrangian frame on a finite element mesh and the global mass density can then be written as a sum of point masses M^p by use of the Dirac delta function,

$$\rho(\mathbf{x}) = \sum_{p=1}^{n^p} M^p \delta(\mathbf{x} - \mathbf{X}^p)\,. \tag{4}$$

The superscript p indicates a material point which is endowed with a fixed mass M^p, a position $\mathbf{X}^p$, a stress $\boldsymbol{\sigma}(\mathbf{X}^p)$ and specific material parameters. Specific to our FSI problem, elements can be mixed, i.e. composed of both solid and fluid phases. However, material points are either solid or fluid. Hence, the finite collection of material points n^p gathers both the fluid material points n_f^p and the solid ones n_s^p, i.e. $n^p = n_f^p + n_s^p$. As a consequence, the grid forces accumulate the internal forces from both phases,

$$\mathbf{f}_i \propto \sum_{p=1}^{n_f^p} M^p \mathrm{div}\, \bar{\boldsymbol{\sigma}}_f(\mathbf{X}^p) + \sum_{p=1}^{n_s^p} M^p \mathrm{div}\, \bar{\boldsymbol{\sigma}}_s(\mathbf{X}^p) = \sum_{p=1}^{n^p} M^p \mathrm{div}\, \bar{\boldsymbol{\sigma}}(\mathbf{X}^p)\,. \tag{5}$$

3 Method of solution

Problems of incompressibility are well known to introduce numerical difficulties, such as mesh locking, in finite element (FE). The numerous solutions developed in the realm of fluid mechanics are summarized in the comprehensive reviews of [7, 11]. A review of those methods is beyond the scope of this paper. Rather, a simple approach is tested here within the MPM and prove quite effective for our purpose (See section 4). This approach assumes a nearly incompressible fluid and uses the assumed strain method [21]. The weak form of the problem, specified to FSI problems and the MPM, is summarized below.

First, let's assume strain and stress discontinuity across the grid elements [25] holding fluid particles. The key point is to use a three-field variational formulation for the fluid domain Ω_f and a standard formulation for the solid domain Ω_s. Regarding the fluid phase we introduce the following enhanced forms of the strain rate field $\dot{\boldsymbol{\epsilon}}$ and the strain rate variation field $\boldsymbol{\gamma}$,

$$\begin{array}{rcccl} \dot{\boldsymbol{\epsilon}} & = & \nabla^* \mathbf{v} & + & \tilde{\dot{\boldsymbol{\epsilon}}} \\ \boldsymbol{\gamma} & = & \nabla^* (\delta \mathbf{v}) & + & \tilde{\boldsymbol{\gamma}} \end{array} \tag{6}$$

in which $\nabla^* \mathbf{v}$ is the symmetric gradient of the velocity field $\mathbf{v}$ and $\delta \mathbf{v}$ is the velocity variation field. Within the three-field formulation, two stresses are introduced: $\boldsymbol{\sigma}$ the actual stress tensor and $\boldsymbol{\sigma}^{\boldsymbol{\epsilon}}$ the stress tensor which

satisfies the constitutive equation $(2)_2$. In addition, $\delta\boldsymbol{\sigma}$ is the stress variation field. Next, we consider the three standard variational equations:

$$\begin{aligned}\int_{\Omega} \delta\mathbf{v} \cdot (\operatorname{div}\boldsymbol{\sigma} + \rho\mathbf{b} - \rho\mathbf{a})\, \mathrm{d}\Omega = 0,\\ \int_{\Omega_f} \delta\boldsymbol{\sigma} \cdot (\nabla^*\mathbf{v} - \dot{\boldsymbol{\epsilon}})\, \mathrm{d}\Omega_f = 0,\\ \int_{\Omega_f} \boldsymbol{\gamma} \cdot \left(-\boldsymbol{\sigma} + \boldsymbol{\sigma}^{\boldsymbol{\epsilon}}\right)\, \mathrm{d}\Omega_f = 0.\end{aligned} \tag{7}$$

A modified form of this latter formulation is obtained by performing a series of steps: integrate by part the divergence term and use the divergence theorem, split the obtained stress term in two parts related to Ω_s and Ω_f, substitute eq. $(6)_1$ into $(7)_2$ and $(6)_2$ into $(7)_3$, and acknowledge that the standard strain rate variation $\nabla^*(\delta\mathbf{v})$ and the enhanced strain rate variation $\tilde{\boldsymbol{\gamma}}$ are independent [21]. Finally, by following the second idea of the assumed strain method [21], the explicit presence of the stress term (within the fluid domain) is eliminated from the modified three-field variational formulation by choosing the space of the stress field L_2-orthogonal to the space of enhanced strains. As a result, the following modified three-field variational problem writes,

$$\begin{aligned}&\int_{\Omega_s} \nabla^*(\delta\mathbf{v}) : \boldsymbol{\sigma}\, \mathrm{d}\Omega_s + \int_{\Omega_f} \nabla^*(\delta\mathbf{v}) : \boldsymbol{\sigma}^{\boldsymbol{\epsilon}}\, \mathrm{d}\Omega_f + \int_{\Omega} \delta\mathbf{v} \cdot \rho\mathbf{a}\, \mathrm{d}\Omega = \\ &\int_{\Omega} \delta\mathbf{v} \cdot \rho\mathbf{b}\, \mathrm{d}\Omega + \int_{\Gamma_s^t} \delta\mathbf{v} \cdot \mathbf{t}\, \mathrm{d}\Gamma_s^t.\\ &\int_{\Omega_f} \tilde{\boldsymbol{\gamma}} \cdot \boldsymbol{\sigma}^{\boldsymbol{\epsilon}}\, \mathrm{d}\Omega_f = 0.\end{aligned} \tag{8}$$

in which $\boldsymbol{\sigma}_s \cdot \mathbf{n} = \mathbf{t}$ on $\partial\Omega_s^t$ and $\mathbf{n}$ is the unit vector outward normal to the boundary. Specific to this FSI framework, no distinction is introduced between the actual stress tensor of the solid phase and the stress tensor which satisfies the constitutive equation $(2)_1$.

The following development follows the standard MPM approach [23]. The substitutions of eq. (4) into eq. (8) convert integrals to sums of quantities evaluated at material points,

$$
\begin{aligned}
&\sum_{p=1}^{n_s^p} \frac{M^p}{\rho^p} \nabla^*(\delta\mathbf{v})|_{\mathbf{x}=\mathbf{X}^p} : \boldsymbol{\sigma}(\mathbf{X}^p) + \sum_{p=1}^{n_f^p} \frac{M^p}{\rho^p} \nabla^*(\delta\mathbf{v})|_{\mathbf{x}=\mathbf{X}^p} : \boldsymbol{\sigma}^{\boldsymbol{\epsilon}}(\mathbf{X}^p) \\
&+ \sum_{p=1}^{n^p} M^p \delta\mathbf{v}(\mathbf{X}^p) \cdot \mathbf{a}(\mathbf{X}^p) = \sum_{p=1}^{n^p} M^p \delta\mathbf{v}(\mathbf{X}^p) \cdot \mathbf{b}(\mathbf{X}^p) + \int_{\Gamma_s^t} \delta\mathbf{v} \cdot \mathbf{t} \, \mathrm{d}\Gamma_s^t \\
&\sum_{p=1}^{n_f^p} \frac{M^p}{\rho_f} \tilde{\boldsymbol{\gamma}}(\mathbf{X}^p) \cdot \boldsymbol{\sigma}^{\boldsymbol{\epsilon}}(\mathbf{X}^p) = 0.
\end{aligned}
\tag{9}
$$

The Galerkin method is adopted for the spatial discretization of variables and test functions. The spatial discretization uses an enhanced strain element. Each element is endowed with four displacement nodes and five enhanced strain nodes (Q1E5) [21]. A grid of isoparametric quadrilateral elements is used to define standard nodal basis functions, $\mathbf{N}_u(\mathbf{x})$, with n_u^n being the total number of displacement nodes,

$$
\begin{aligned}
&\delta\mathbf{u}(\mathbf{x}) = \sum_{i=1}^{n_u^n} \delta\mathbf{u}_i^e N_u^i(\mathbf{x}) = \mathbf{N}_u(\mathbf{x}) \, \delta\mathbf{u}^e, \quad \delta\mathbf{v}(\mathbf{x}) = \mathbf{N}_u(\mathbf{x}) \, \delta\mathbf{v}^e, \\
&\mathbf{u}(\mathbf{x}) = \mathbf{N}_u(\mathbf{x}) \, \mathbf{u}^e, \quad \mathbf{v}(\mathbf{x}) = \mathbf{N}_u(\mathbf{x}) \, \mathbf{v}^e, \quad \mathbf{a}(\mathbf{x}) = \mathbf{N}_u(\mathbf{x}) \, \mathbf{a}^e \\
&\tilde{\boldsymbol{\gamma}}(\mathbf{x}) = \mathbf{G}(\mathbf{x}) \, \tilde{\boldsymbol{\gamma}}^e, \quad \tilde{\dot{\boldsymbol{\epsilon}}}(\mathbf{x}) = \mathbf{G}(\mathbf{x}) \, \tilde{\dot{\boldsymbol{\epsilon}}}^e,
\end{aligned}
\tag{10}
$$

while $\mathbf{G}(\mathbf{x})$ is the enhanced strain rate interpolation matrix of size 5×4, for a 2D plain strain problem. $\delta\mathbf{u}_i^e$, $\delta\mathbf{v}^e$, $\mathbf{u}_i^e$, $\mathbf{v}_i^e$, $\mathbf{a}_i^e$, $\tilde{\boldsymbol{\gamma}}^e$ and $\tilde{\dot{\boldsymbol{\epsilon}}}^e$ denote the nodal vectors of the approximated functions.

For an arbitrary field $\delta\mathbf{v}^e$ and by use of definitions $(2)_2$ and $(6)_1$, the fluid contribution to the internal force vector may be expressed as,

$$
\begin{aligned}
\sum_{p=1}^{n_f^p} V^p \mathbf{B}^{\mathrm{T}}(\mathbf{X}^p) \boldsymbol{\sigma}_f^{\boldsymbol{\epsilon}}(\mathbf{X}^p) &= \sum_{p=1}^{n_f^p} V^p \mathbf{B}^{\mathrm{T}}(\mathbf{X}^p) \mathbf{T}_f \left(\nabla^* \mathbf{v}(\mathbf{X}^p) + \tilde{\dot{\boldsymbol{\epsilon}}}(\mathbf{X}^p) \right) \\
&= \sum_{p=1}^{n_f^p} V^p \mathbf{B}^{\mathrm{T}}(\mathbf{X}^p) \mathbf{T}_f \left(\mathbf{B}(\mathbf{X}^p) \mathbf{v}^e + \mathbf{G}(\mathbf{X}^p) \, \tilde{\dot{\boldsymbol{\epsilon}}}^e \right)
\end{aligned}
\tag{11}
$$

in which $\mathbf{B}(\mathbf{X}^p) = \nabla \mathbf{N}_u(\mathbf{x})|_{\mathbf{x}=\mathbf{X}^p}$ is the strain displacement matrix evaluated at $\mathbf{X}^p$. Finally, the matrix form of the system is obtained for the arbitrary components $\delta\mathbf{v}^e$ and $\tilde{\boldsymbol{\gamma}}^e$,

$$\begin{aligned} \mathbf{K}^e(\mathbf{X}^p)\,\mathbf{u}^e + \mathbf{D}^e(\mathbf{X}^p)\,\mathbf{v}^e + \mathbf{M}^e(\mathbf{X}^p)\,\mathbf{a}^e + (\boldsymbol{\Gamma}^e(\mathbf{X}^p))^{\mathrm{T}}\tilde{\dot{\boldsymbol{\epsilon}}}^e &= \mathbf{F}^e_{\mathbf{v}}(\mathbf{X}^p) \\ &+ \boldsymbol{\Theta}^e(\mathbf{x}), \\ \boldsymbol{\Gamma}^e(\mathbf{X}^p)\,\mathbf{v}^e \qquad\qquad + \mathbf{H}^e(\mathbf{X}^p)\;\tilde{\dot{\boldsymbol{\epsilon}}}^e &= 0, \end{aligned} \tag{12}$$

in which we have introduced the discrete stiffness matrix $\mathbf{K}^e(\mathbf{X}^p)$, the discrete diffusion matrix $\mathbf{D}^e(\mathbf{X}^p)$, the discrete mass matrix $\mathbf{M}^e(\mathbf{X}^p)$, the discrete coupled matrix $\boldsymbol{\Gamma}^e(\mathbf{X}^p)$, the discrete body force vector $\mathbf{F}^e_{\mathbf{v}}(\mathbf{X}^p)$, the discrete traction vector $\boldsymbol{\Theta}^e(\mathbf{x})$ and the discrete enhanced strain rate matrix $\mathbf{H}^e(\mathbf{X}^p)$. The definitions of those matrices are given in Appendix A.

The system of equations (12), which is a compact system of $(n_{dim} \times n^n_u + n^n_{\boldsymbol{\epsilon}})$ equations and unknowns, is solved fully implicitly by use of a standard Newmark scheme and a Newton Raphson procedure. The obtained formulation is further condensed out so that the enhanced strain unknowns disappear. It is proposed that the obtained formulation be simulated with the MPM. The idea is straightforward in that the algorithm is setup as any other type of MPM simulation. More details on the complete algorithm can be found in the following seminal references [23, 24].

4 Results and discussions

The potentials of the proposed method are highlighted with three numerical simulations, in two-dimensions. First a fluid flow around a cylindrical obstacle demonstrates the performance of the proposed algorithm for incompressible fluids. Next, the method is tested for problems involving free surfaces. The classic results of a collapsing water column are compared with experimental and XFEM numerical data. Finally, the accuracy of the method is tested on a sedimentation test. It was found that the results obtained with the MPM are more accurate than those of an immersed boundary method.

4.1 Fluid flow around a cylindrical obstacle

To test the properties of the model for an incompressible fluid, several calculations are performed by using a fixed elastic but very stiff obstacle. Fluid flow is scrutinized past a unit-radius (r) cylindrical obstacle located at the

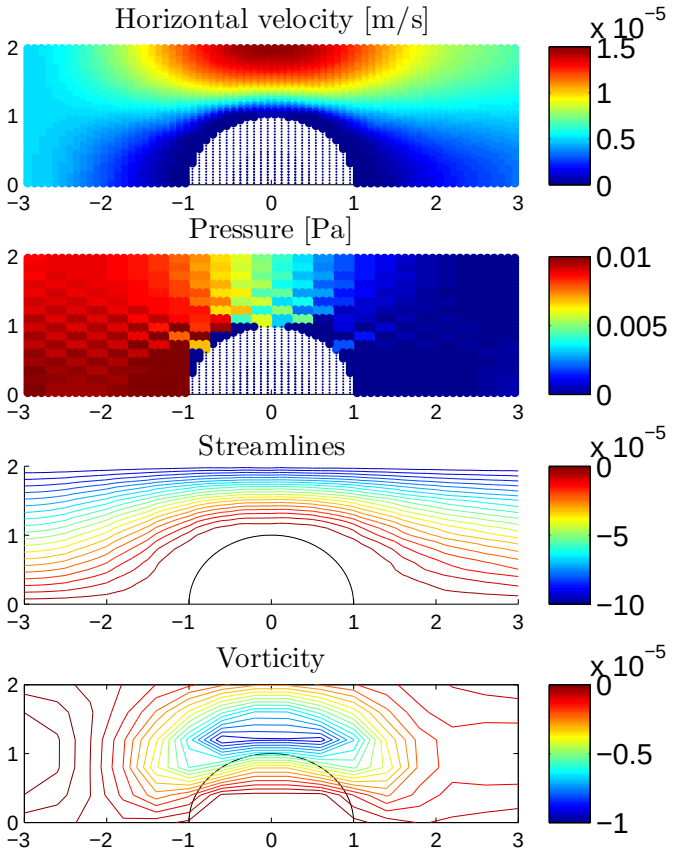

Figure 1: The particles defining the incompressible fluid and the obstacle along an axis of symmetry are shown for a 24×16 grid with 9 MPs per Q1E5 element. The horizontal velocity and the pressure contours reflect the good capabilities of the method, while the streamlines and the vorticity are characteristic of 'sticky' Stokes flows.

center of the following domain $-3 \leq x \leq 3$ and $-2 \leq y \leq 2$ [7]. The symmetry of the setup allows us to restrict ourselves to the upper half of the domain. The boundary conditions are as follows: $\mathrm{v}_x = \mathrm{v}_0 f(t/t_{\mathrm{endload}})$ and $\mathrm{v}_y = 0$ at the inlet ($x = -3$) with $f(x) = x^3 * (10 - 15 * x + 6 * x^2)$ for $x < 1$, $f(x) = 1$ for $x \geq 1$ and t_{endload} being the acceleration time constant; traction free boundary conditions at the outlet ($x = 3$) and symmetry elsewhere ($y = 0$ and $y = 2$) with $\mathrm{v}_y = 0$. Initial velocities assume a no-flow configuration. The time step in the Newton Raphson scheme is chosen as

$\Delta t = 0.001\,\mathrm{s}$. The characteristic lengths defining the Reynolds number are $\mathrm{v}_0 = 5 \times 10^{-6}\,\mathrm{m/s}$, $\nu_f = 0.1\,\mathrm{m}^2/\mathrm{s}$ and $r = 1\,\mathrm{m}$. The flow regime is hence close to a Stokes flow.

The calculated response is examined to test linear stability (Figure 1). The particles defining the incompressible fluid and the obstacle are attached to a 24×16 uniform grid on which the system (12) solved. Both the horizontal velocity and the pressure contours are reasonable, the latter being symmetric about $x = 0$ and close to zero at the exit [7]. Note that the pressure solution in mixed elements (in the vicinity of the obstacle) is inaccurate highlighting the limit of the method. The streamlines in Figure 1 show the 'large' displacement thickness characteristic of 'sticky' Stokes flows; while the vorticity has diffused in a nearly-symmetric shape.

Clearly, the classical FEM would lead to results of greater quality in the vicinity of the obstacle to the price of adapting the mesh to this obstacle. A similar result, would be obtained with the MPM and an unstructured mesh that respects the boundary of the obstacle. Yet the aim here is to show that even with an unstructured coarse mesh consisting of 24×16 elements, the MPM can provide sufficiently accurate results.

4.2 A collapsing water column

This test case considers a domain of size $0.584\,\mathrm{m} \times 0.45\,\mathrm{m}$ containing a water column on the left-hand-side of size $a \times b = 0.146\,\mathrm{m} \times 0.292\,\mathrm{m}$ [6, 14]. While the water properties are $\rho_f = 1000\,\mathrm{kg/m}^3$ and $\mu_f = 1 \times 10^{-3}\,\mathrm{Pa.s}$, the rest of the domain is filled with an incompressible fluid endowed with the following properties $\rho = 1\,\mathrm{kg/m}^3$ and $\mu = 1 \times 10^{-5}\,\mathrm{Pa.s}$, representing air. No surface tension is considered. The loading is merely restricted to a volumetric gravitation force $g = -9.81\,\mathrm{m/s}^2$. Free-slip boundary conditions are assumed along the boundaries of the domain. Two meshes are used, consisting of 12×9 and 36×27 elements. Each mesh is endowed with 36 MPs per cell and the simulation time is restricted to $0.3\,\mathrm{s}$ with $\Delta t = 3 \times 10^{-4}\,\mathrm{s}$.

The water column positions and pressure contour at some selected points in time are compared in Figure 2. The evolutions of the dimensionless water column width and height with dimensionless times are compared with experimental data [14] and the intrinsic XFEM solution [6] in Figure 3. Dimensionless displacements and times are defined as follows,

$$w^* = \frac{w}{a}, \qquad h^* = \frac{h}{b}, \qquad \tau_w = t\sqrt{\frac{2g}{a}}, \qquad \tau_h = t\sqrt{\frac{2g}{b}} \tag{13}$$

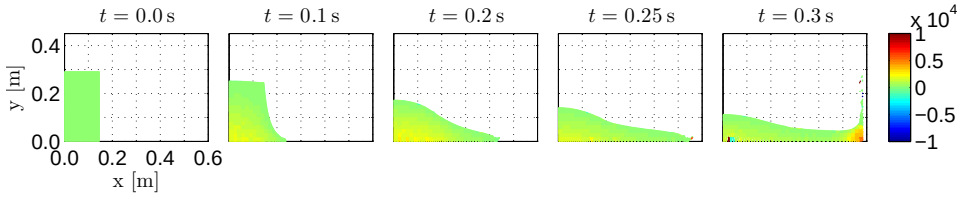

Figure 2: Water column position and pressure contour at 5 selected times for the Q1E5 element. The 36×27 elements mesh uses 36 MPs per cell.

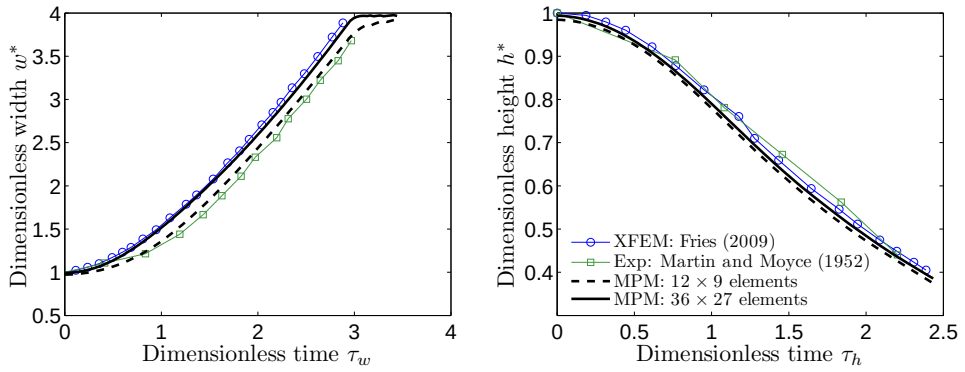

Figure 3: Dimensionless (left) width and (right) height over time, see eq. (13), for the collapsing water column test case. Each MPM mesh uses 36 MPs per cell. The MPM solution agrees well with other results in spite of the coarse nature of the meshes.

in which w and h correspond to the intersection points of the water column interface with the bottom and left walls of the domain, respectively, so that at $t = 0$, $w^* = h^* = 1$. An excellent agreement of the MPM solution with other results is found where classical FEM results are known to be unsatisfactory [6].

4.3 Sedimentation test

This last test case mimics the sedimentation of a deformable cylinder in an incompressible fluid. We calculate the motion of the circular cylinder of radius a in between two parallel walls, of width $2L = 2.0\,\mathrm{m}$. The motion of the cylinder, directed perpendicular to its axis with its axis positioned midway between the walls, is solely induced by gravity $g = -9.81\,\mathrm{m/s^2}$. The cylinder properties are $\rho_s = 2700\,\mathrm{kg/m^3}$, $E_s = 36\,\mathrm{GPa}$ and $\nu_s = 0.25$ and

the incompressible fluid properties are $\rho_f = 1000\,\mathrm{kg/m^3}$ and $\mu_f = 1000\,\mathrm{Pa.s}$. The boundary conditions assume zero vertical and horizontal velocities on the vertical boundaries and zero vertical velocities only on the horizontal boundaries. The time step in the Newton Raphson scheme is chosen as $\Delta t = 0.001\,\mathrm{s}$.

For a cylinder settling along the axis of an infinite channel, Faxen [3] presents a close form solution for small a/L that relates the ratio a/L to the steady state vertical velocity v_y^∞ (reported in Happel and Brenner [9], p. 345). This theory is compared to MPM simulations and to the work of Sulsky and Brackbill [22] for cylinders of various radius in Table 1.

The results are in agreement with the approximated theory [3] and the error remains small for $a/L < 0.5$. By using a modified immersed boundary technique, Sulsky and Brackbill [22] report an error decreasing in magnitude with increased resolution of the cylinder ($a/\Delta x$) and increasing in magnitude up to 10% error with $a/L = 0.4$. In comparison, the error on the MPM solution seems less dependent of the mesh resolution and is most probably due to the influence of mixed elements.

a/L	$a/\Delta x$	v_y^∞ [m/s] theory	v_y^∞ [m/s] MPM	error% MPM	error% Sulsky and Brackbill [22]
0.1	5	0.0585	0.0591	-0.96	1.8
0.2	10	0.1267	0.1263	0.38	2.6
0.3	15	0.1611	0.1594	1.05	-0.8
0.4	20	0.1549	0.1557	-0.52	-10.5

Table 1: Velocity comparison of a settling cylinder between two rigid walls computed on a 50×100 grid with 9 MPs per cell. In comparison with the results of Sulsky and Brackbill [22], the MPM response is less dependent on the mesh resolution ($a/\Delta x$) and remains accurate within $\approx 1\,\%$ for $a/L \leq 0.4$.

5 Conclusion

The MPM is applied to the interaction of incompressible fluids and deformable particles. This method uses Lagrangian material points and an

Eulerian grid or mesh to define the computational domain. The material points move through the Eulerian grid on which the balance equations are solved. This paper presents the modifications necessary to simulate the interactions between incompressible fluids and solid materials by using the assumed strain method. The spacial discretisation uses an enhanced strain element (Q1E5) [21].

Several two-dimensional test problems are presented to demonstrate the methodology. A fluid flow test past an obstacle is used to test the incompressible fluid model, for Stokes flows. The method performs well despite the fact that the mesh does not fit the obstacle. Next, a collapsing water column test is presented to evaluate the accuracy of the method. The MPM response compares very well with both experimental [14] and XFEM results [15]. Finally, a sedimentation test is performed to validate the fluid-solid interactions. Again the proposed method performs well with respect to the analytical solution [3] and better than other numerical methods such as the modified immersed boundary formulation [22].

The enhanced strain element Q1E5 used throughout this paper matches well the MPM procedure since it is compatible with the use of a lumped mass matrix during the initialization step. Yet this element does not satisfy of the inf-sup test so that one possible extension of the method is to test other elements such as the combined mixed displacement/pressure enhanced finite element [18]. Also the proposed element does not satisfy strictly the incompressibility condition $\operatorname{div} \mathbf{v} = 0$ and the results presented herein will be compared in a near future with that obtained with a bi-linear mixed element Q1P0 [7].

Acknowledgments

The authors would like to thank the Australian Research Council for the Discovery Projects funding scheme (project DP110102645).

A Discrete matrices used in eq. (12)

The discrete coupled matrix $\mathbf{\Gamma}^e(\mathbf{X}^p)$, the discrete diffusion matrix $\mathbf{D}^e(\mathbf{X}^p)$, and the discrete enhanced strain rate matrix $\mathbf{H}^e(\mathbf{X}^p)$ write,

$$
\begin{aligned}
\mathbf{\Gamma}^e(\mathbf{X}^p) &= \sum_{p=1}^{n_f^p} V^p \mathbf{G}^{\mathrm{T}}(\mathbf{X}^p)\mathbf{T}_f\mathbf{B}(\mathbf{X}^p),\\
\mathbf{D}^e(\mathbf{X}^p) &= \sum_{p=1}^{n_f^p} V^p \mathbf{B}^{\mathrm{T}}(\mathbf{X}^p)\mathbf{T}_f\mathbf{B}(\mathbf{X}^p),\\
\mathbf{H}^e(\mathbf{X}^p) &= \sum_{p=1}^{n_f^p} V^p \mathbf{G}^{\mathrm{T}}(\mathbf{X}^p)\ \mathbf{T}_f\ \mathbf{G}(\mathbf{X}^p).
\end{aligned}
\tag{14}
$$

Also we have introduced the discrete mass matrix $\mathbf{M}^e(\mathbf{X}^p)$, the discrete body force vector $\mathbf{F}^e_{\mathbf{v}}(\mathbf{X}^p)$, the discrete traction vector $\mathbf{\Theta}^e(\mathbf{x})$ and the discrete stiffness matrix $\mathbf{K}^e(\mathbf{X}^p)$ as,

$$
\begin{aligned}
\mathbf{M}^e(\mathbf{X}^p) &= \sum_{p=1}^{n^p} M^p \mathbf{N}_u^{\mathrm{T}}(\mathbf{X}^p)\mathbf{N}_u(\mathbf{X}^p),\\
\mathbf{F}^e_{\mathbf{v}}(\mathbf{X}^p) &= \sum_{p=1}^{n^p} M^p \mathbf{N}_u^{\mathrm{T}}(\mathbf{X}^p)\mathbf{b}(\mathbf{X}^p),\\
\mathbf{\Theta}^e(\mathbf{x}) &= \int_{\Gamma_s^t} \mathbf{N}_u^{\mathrm{T}}(\mathbf{x})\ \mathbf{t}\ \mathrm{d}\Gamma_s^t,\\
\mathbf{K}^e(\mathbf{X}^p) &= \sum_{p=1}^{n_s^p} V^p \mathbf{B}^{\mathrm{T}}(\mathbf{X}^p)\ \mathbf{T}_s\ \mathbf{B}(\mathbf{X}^p)
\end{aligned}
\tag{15}
$$

It is worth noting that the number of integration points used to obtain the various discrete matrices is adapted depending on the nature of each term, i.e. the diffusion, coupled and enhanced strain rate matrices are summed over the fluid material points, the stiffness matrix is summed over the solid material points, and the mass matrix is evaluated using all material points of the element.

References

[1] T. Belytschko, B. Liu, W.K.and Moran, and K. Elkhodary. *Nonlinear finite elements for continua and structures*. John Wiley & Sons, 2013.

[2] H.H. Bui, K. Sako, and R. Fukagawa. Numerical simulation of soil–water interaction using smoothed particle hydrodynamics (sph) method. *Journal of Terramechanics*, 44(5):339–346, 2007.

[3] H. Faxen. Hydrodynamical resistance formula. *Neuvième Congrès des mathématiciens scandinaves à Helsingfors du 23 au 26 août 1938*, 1(9):165, 1939.

[4] R. Fell and J.J. Fry. *Internal erosion of dams and their foundations*. Taylor & Francis, Oxon, Royaume Uni, 2007.

[5] T.-P. Fries and H.-G. Matthies. Classification and overview of meshfree methods. Technical report, Institute of Scientific Computing Technical University Braunschweig Brunswick, Germany, 2004.

[6] T.P. Fries. The intrinsic xfem for two-fluid flows. *International Journal for Numerical Methods in Fluids*, 60(4):437–471, 2009.

[7] P.M. Gresho and R.L. Sani. *Incompressible flow and the finite element method. Volume 1: Advection-diffusion and isothermal laminar flow*. John Wiley and Sons, Inc., New York, NY (United States), 1998.

[8] I. Guiamatsia and G.D. Nguyen. Crack modelling using the material point method and a strong discontinuity approach. In *Key Engineering Materials*, volume 525, pages 513–516. Trans Tech Publ, 2013.

[9] H. Happel, J.and Brenner. *Low Reynolds number hydrodynamics: with special applications to particulate media*, volume 1. Springer Science & Business Media, 1983.

[10] S. Ii, K. Sugiyama, S. Takeuchi, S. Takagi, and Y. Matsumoto. An implicit full eulerian method for the fluid-structure interaction problem. *International Journal for Numerical Methods in Fluids*, 65(1-3):150–165, 2011.

[11] H.P. Langtangen, K.-A. Mardal, and R. Winther. Numerical methods for incompressible viscous flow. *Advances in Water Resources*, 25(8):1125–1146, 2002.

[12] F. Lominé, L. Scholtès, L. Sibille, and P. Poullain. Modeling of fluid–solid interaction in granular media with coupled lattice boltzmann/discrete element methods: application to piping erosion. *International Journal for Numerical and Analytical Methods in Geomechanics*, 37(6):577–596, 2013.

[13] E Love and DL Sulsky. An energy-consistent material-point method for dynamic finite deformation plasticity. *International Journal for Numerical Methods in Engineering*, 65(10):1608–1638, 2006.

[14] J.C. Martin and W.J. Moyce. An experimental study of the collapse of liquid columns on a rigid horizontal plane. *Philosophical Transactions of the Royal Society of London. Series A, Mathematical and Physical Sciences*, 244(882):312–324, 1952.

[15] J.E. Mindel. *Interface tracking and solid-fluid coupling techniques with coastal engineering applications*. PhD thesis, Imperial College London, 2008.

[16] G.D. Nguyen. An enriched constitutive model for fracture propagation analysis using the material point method. *Applied Mechanics and Materials*, 553:731–736, 2014.

[17] E. Oñate, S.R. Idelsohn, M.A. Celigueta, and R. Rossi. Advances in the particle finite element method for the analysis of fluid–multibody interaction and bed erosion in free surface flows. *Computer Methods in Applied Mechanics and Engineering*, 197(19):1777–1800, 2008.

[18] D. Pantuso and K.-J. Bathe. A four-node quadrilateral mixed-interpolated element for solids and fluids. *Mathematical models and methods in applied sciences*, 5(08):1113–1128, 1995.

[19] E. Papamichos and I. Vardoulakis. Sand erosion with a porosity diffusion law. *Computers and Geotechnics*, 32(1):47–58, 2005.

[20] P. Rognon and C. Gay. Soft dynamics simulation. 1. normal approach of two deformable particles in a viscous fluid and optimal-approach strategy. *The European Physical Journal E: Soft Matter and Biological Physics*, 27(3):253–260, 2008.

[21] J.C. Simo and M.S. Rifai. A class of mixed assumed strain methods and the method of incompatible modes. *International Journal for Numerical Methods in Engineering*, 29(8):1595–1638, 1990.

[22] D. Sulsky and J.U. Brackbill. A numerical method for suspension flow. *Journal of Computational Physics*, 96(2):339–368, 1991.

[23] D. Sulsky, Z. Chen, and H.L. Schreyer. A particle method for history-dependent materials. *Computer Methods in Applied Mechanics and Engineering*, 118(1):179–196, 1994.

[24] D. Sulsky, S.-J. Zhou, and H.L. Schreyer. Application of a particle-in-cell method to solid mechanics. *Computer physics communications*, 87(1):236–252, 1995.

[25] K. Washizu. *Variational methods in elasticity and plasticity*. Pergamon Press, New York, 1982.

[26] A.R. York, D. Sulsky, and H.L. Schreyer. Fluid–membrane interaction based on the material point method. *International Journal for Numerical Methods in Engineering*, 48(6):901–924, 2000.